AGU PUBLICATIONS

JGR

Journal of Geophysical Research: Atmospheres

RESEARCH ARTICLE

10.1002/2017JD027752

**Key Points:**
- Nonspherical snow grains tend to have higher albedos but lower BC-induced albedo reductions than spherical counterparts
- Multiple BC-snow internal mixing reduces snow albedo more than external mixing by a factor of 1.2–2.0 depending on BC content and snow shape
- Snow albedo parameterizations have been developed to account for the effects of snow grain shape and multiple BC-snow internal mixing

**Supporting Information:**
- Supporting Information S1
- Data Set S1

**Correspondence to:**
C. He,
cenlinhe@atmos.ucla.edu

**Citation:**
He, C., Liou, K.-N., Takano, Y., Yang, P., Qi, L., & Chen, F. (2018). Impact of grain shape and multiple black carbon internal mixing on snow albedo: Parameterization and radiative effect analysis. *Journal of Geophysical Research: Atmospheres*, *123*, 1253–1268. https://doi.org/10.1002/2017JD027752

Received 19 SEP 2017
Accepted 2 JAN 2018
Accepted article online 6 JAN 2018
Published online 24 JAN 2018



# Impact of Grain Shape and Multiple Black Carbon Internal Mixing on Snow Albedo: Parameterization and Radiative Effect Analysis

**Cenlin He[1,2], Kuo-Nan Liou[1], Yoshi Takano[1], Ping Yang[3], Ling Qi[4], and Fei Chen[2]**

[1]Joint Institute for Regional Earth System Science and Engineering, and Department of Atmospheric and Oceanic Sciences, University of California, Los Angeles, CA, USA, [2]National Center for Atmospheric Research, Boulder, CO, USA, [3]Department of Atmospheric Sciences, Texas A&M University, College Station, TX, USA, [4]School of Environment, Tsinghua University, Beijing, China

**Abstract** We quantify the effects of grain shape and multiple black carbon (BC)-snow internal mixing on snow albedo by explicitly resolving shape and mixing structures. Nonspherical snow grains tend to have higher albedos than spheres with the same effective sizes, while the albedo difference due to shape effects increases with grain size, with up to 0.013 and 0.055 for effective radii of 1,000 μm at visible and near-infrared bands, respectively. BC-snow internal mixing reduces snow albedo at wavelengths $<$ ~1.5 μm, with negligible effects at longer wavelengths. Nonspherical snow grains show less BC-induced albedo reductions than spheres with the same effective sizes by up to 0.06 at ultraviolet and visible bands. Compared with external mixing, internal mixing enhances snow albedo reduction by a factor of 1.2–2.0 at visible wavelengths depending on BC concentration and snow shape. The opposite effects on albedo reductions due to snow grain nonsphericity and BC-snow internal mixing point toward a careful investigation of these two factors simultaneously in climate modeling. We further develop parameterizations for snow albedo and its reduction by accounting for grain shape and BC-snow internal/external mixing. Combining the parameterizations with BC-in-snow measurements in China, North America, and the Arctic, we estimate that nonspherical snow grains reduce BC-induced albedo radiative effects by up to 50% compared with spherical grains. Moreover, BC-snow internal mixing enhances the albedo effects by up to 30% (130%) for spherical (nonspherical) grains relative to external mixing. The overall uncertainty induced by snow shape and BC-snow mixing state is about 21–32%.

**Plain Language Summary** Pure snow strongly reflects sunlight, the degree of which is regulated by grain size and shape. Observations have shown that snow can be significantly darkened by impurities, such as black carbon (BC), which is the most important light-absorbing aerosol. However, the combined effects of the two critical factors, snow grain shape and BC-snow mixing structure, have not been previously investigated, the neglect of which could introduce large uncertainties in the estimates of snow albedo in terms of BC-induced darkening. We have developed a snow model to quantify the impact of the preceding two factors on snow albedo by means of resolving the structures of BC-snow mixtures for different grain shapes. Both snow grain shape and multiple BC-snow internal mixing play important roles in their impacts on snow albedo. For application to climate models, we construct a scheme to parameterize snow albedo and its darkening in terms of snow grain size, shape, and BC content.

## 1. Introduction

Snow albedo is a key climate parameter that significantly affects surface energy balance in the Earth system. Reduction of snow albedo enhances surface warming (Hansen & Nazarenko, 2004; Qian et al., 2009), accelerates snow melting (Menon et al., 2010; Ming et al., 2015), and further alters large-scale hydrological cycle (Qian et al., 2009, 2011). Ample evidences have revealed significant snow albedo reductions associated with impurity contamination (e.g., Dang et al., 2017, Lee et al., 2017, Qian et al., 2015), in particular black carbon (BC), the most important light-absorbing aerosol (Bond et al., 2013; Painter et al., 2013). Moreover, snow grain properties, including size, shape, and packing structures, can further influence snow albedo and its reduction caused by BC (e.g., Flanner et al., 2007; He et al., 2014; He, Takano, & Liou, 2017; Kokhanovsky, 2013; Kokhanovsky & Zege, 2004; Liou et al., 2014; Räisänen et al., 2017; Warren & Wiscombe, 1980). Thus, quantifying the effects of both BC and snow grain properties is critical to accurate predictions of snow albedo and associated climatic impact.

In the past few decades, substantial efforts have been made to improve modeling of snow albedo altered by impurity. For example, Wiscombe and Warren (1980) developed a radiative transfer model for pure snow by assuming spherical snow grains. Warren and Wiscombe (1980) further accounted for BC contamination in snow by assuming BC-snow external mixing and found a decrease of up to 15% in visible albedo caused by 1 ppm BC in snow. Using this model and BC-in-snow measurements, Warren and Wiscombe (1985) estimated a spectrally averaged BC-induced snow albedo reduction of up to 0.015 and 0.035 for fresh and aged snow over the Arctic, respectively. Following the work of Warren and Wiscombe (1980), Flanner et al. (2007) developed a more sophisticated multilayer snow albedo model (SNICAR) that includes a dynamic snow aging process and the effect of impurities externally mixed with snow spheres. They showed annual BC-induced area-mean Arctic albedo reductions (including the effects of both reduced snow cover and albedo) of 0.047 and 0.017 in strong and weak boreal fire years, respectively. Recently, Aoki et al. (2011) developed a physically based multilayer snow albedo model (PBSAM) to account for external mixing of impurity involving spherical snow grains and snow aging.

In addition, for application to climate models, a number of snow albedo parameterizations have been developed by assuming spherical snow grains externally mixed with impurities. Marshall and Warren (1987) showed that snow albedo can be parameterized by snow depth, grain size, BC concentration, and environmental variables (e.g., solar zenith angle, cloud transmittance, and underlying ground albedo), which has been implemented in a global climate model (Marshall & Oglesby, 1994). Gardner and Sharp (2010) developed a theoretically based parameterization for broadband snow albedo as a function of solar zenith angle, snow depth, cloud optical depth, specific snow surface area, and BC concentration. Dang et al. (2015) recently derived a simplified snow albedo parameterization to account for BC-induced albedo reduction depending on BC content and snow grain size.

However, the effects of nonspherical snow shape and multiple BC-snow internal mixing, which are commonly observed in real snowpack (Dominé et al., 2003; Erbe et al., 2003; Flanner et al., 2012; Magono et al., 1979), have not been understood or included in snow models and parameterizations. Kokhanovsky and Zege (2004) found that using spherical snow grains causes substantial errors in snow albedo modeling. They developed an asymptotic analytical radiative transfer (AART) theory for nonspherical grains in a vertically homogeneous snowpack. Fu (2007) showed that asymmetry factors of nonspherical ice crystals are much smaller than those of spheres and formulated a parameterization for hexagonal ice crystals. Using this parameterization, Dang et al. (2016) found higher albedos and less BC-induced albedo reductions for nonspherical snow grains than spherical counterparts by assuming BC-snow external mixing. Flanner et al. (2012) estimated that 32–73% of BC particles in snow are internally mixed with snow grains. They employed a dynamic effective medium approximation approach to quantify the effect of multiple BC particles internally mixed with spherical snow grains and showed up to 86% increase in snow albedo effect caused by internal mixing relative to external mixing. None of these studies, however, have simultaneously accounted for snow grain nonsphericity and BC-snow internal mixing. For this reason, it is imperative to assess the combined effects of both factors in order to accurately estimate snow albedo and BC-induced radiative effects, as well as to derive a physical understanding of their intricate interactions.

Recently, Liou et al. (2014) developed a stochastic snow albedo model to explicitly resolve nonspherical snow grains internally mixed with impurities based on a geometric-optics surface-wave (GOS) approach, which provides a powerful tool for understanding the combined effects of snow grain shape and multiple BC-snow internal mixing. Using Liou et al.'s (2014) model, our previous study (He, Takano, Liou, Yang, et al., 2017) has quantified the impact of both factors on snow single-scattering properties and developed a set of parameterizations for use in climate models.

Further to the study reported in He, Takano, Liou, Yang, et al. (2017), the present study quantifies the impacts of snow grain shape and multiple BC-snow internal mixing on snow albedo. Moreover, we develop for the first time a set of snow albedo parameterizations that simultaneously account for the preceding two factors for applications to land surface and climate models. Combining the parameterizations with BC-in-snow measurements, we further estimate BC-induced snow albedo reductions and associated surface radiative effects over the Northern Hemispheric snowpack as well as the uncertainties caused by snow grain shape and BC-snow mixing state.

## 2. Methods

### 2.1. Single-Scattering Properties of Clean and Dirty Snow

Calculations of the single-scattering properties for clean and BC-contaminated snow have been described and presented in details in He, Takano, Liou, Yang, et al. (2017). Here we provide a brief summary of key elements involved in the computation. We take into account four snow grain shapes (Figure S1 in the supporting information), namely sphere, Koch snowflake, spheroid, and hexagonal plate, with volume-equivalent sphere radii ($R_v$) of 50, 100, 500, 1,000, and 2,000 μm (Table S1). These shapes capture the major morphological characteristics of observed snow grain structures (Dominé et al., 2003; Erbe et al., 2003). The snow size range in this study spans observed values in real snowpack (LaChapelle, 1969; Nakamura et al., 2001). Snow spectral refractive index is from Warren and Brandt (2008). Note that we use $R_v$ to define model scenarios/experiments in order to generate a comprehensive snow albedo data set for further analysis, while we use a parameter defined as snow effective size, rather than $R_v$, in albedo parameterizations (see section 2.3).

For multiple BC-snow internal mixing, we follow a stochastic procedure (Liou et al., 2014) to randomly distribute a number of BC particles inside snow grains in order to reflect the effects of stochastic processes involved in the formation of BC-snow mixtures (Flanner et al., 2012). Even if the BC-snow mixing state changes during snow aging processes and leads to a different distribution of BC particles in a snow grain, BC positions cannot be known to certainty so that the stochastic approach must be followed. We compute the number of BC within each grain based on snow and BC particle sizes, their densities, and BC mass content in snow. We employ BC spheres (after aging processes in the atmosphere) with an effective radius of 0.1 μm (Schwarz et al., 2013). We use densities of 1.7 g $cm^{-3}$ (Bond & Bergstrom, 2006) and 0.917 g $cm^{-3}$ (Wiscombe & Warren, 1980) for BC and ice, respectively, and the BC spectral refractive index presented in Krekov (1993). Based on the observed BC content in snowpack (Qian et al., 2015), BC mass concentrations ($C_{BC}$) of 0, 1, 10, 50, 100, 500, 1,000 ppb (or ng $g^{-1}$) are utilized in this study. We note that extremely high BC concentrations ($C_{BC} > 1{,}000$ ppb) have also been observed over the Northern China snowpack (Wang et al., 2013). For comparison with internal mixing, we have also conducted computations for BC-snow external mixing under the same conditions.

We follow the GOS approach (He et al., 2015, 2016; Liou et al., 2011, 2014) to compute the spectral single-scattering properties (i.e., extinction efficiency, asymmetry factor, and single-scattering albedo) of clean and BC-contaminated snow at wavelengths ($\lambda$) of 0.2–5 μm with an interval of 0.01 μm. The GOS approach explicitly resolves snow grain shapes and BC-snow mixing structures and has been cross validated with lab measurements (He et al., 2015) and other optical methods (He et al., 2016; Liou et al., 2011; Takano et al., 2013). Liou and Yang (2016) provided a comprehensive review of the GOS approach.

### 2.2. Snow Albedo Calculation

We calculate spectral snow albedo using the adding/doubling method (Takano & Liou, 1989a, 1989b) and the precomputed spectral single-scattering properties of clean and contaminated snow (see section 2.1). We assume a homogeneous plane-parallel snowpack with an optically semi-infinite depth. Dang et al. (2016) showed that fresh snowpack deeper than 0.3 m is effectively semi-infinite and that snow albedo is more sensitive to snowpack thickness for aged snow. In the calculations, the underlying ground surface is taken to be black. We use a solar zenith angle of 49.5°, whose cosine value (0.65) represents the insolation-weighted mean solar zenith cosine for sunlit Earth hemisphere (Dang et al., 2015). The snow albedo under other solar zenith angles can be approximated by altering the snow grain size (Marshall, 1989).

Based on the spectral snow albedo, we further compute broadband snow albedo ($\overline{\alpha}$) as follows:

$$\overline{\alpha} = \frac{\int \alpha_\lambda s_\lambda d\lambda}{\int s_\lambda d\lambda} \tag{1}$$

where $\alpha_\lambda$ is the spectral snow albedo and $s_\lambda$ is the incident solar spectrum available from the American Society for Testing and Materials reference data set (see He, Takano, Liou, Yang, et al., 2017 for more details), which approximately represents the mean clear-sky condition in northern midlatitudes. We note that Aoki et al. (2003) found negligible differences between clear- and cloudy-sky conditions for visible snow albedo but a higher near-infrared (NIR) albedo under cloudy sky relative to clear sky.

### 2.3. Parameterization

For a direct application to land surface and climate models, we develop a set of parameterizations for pure snow albedo and BC-induced albedo reduction to account for the effects of snow grain shape and BC-snow internal/external mixing, based on the theoretically computed snow albedo (see section 2.2). We consider four types of solar spectral bands: a broadband type with 3 bands (ultraviolet (UV), visible, and NIR), a Community Land Model (CLM) band type with 5 bands (referred to as CLM bands) (Oleson et al., 2004), a Fu-Liou/Fu-Liou-Gu Radiative Transfer Model band type with 6 bands (referred to as FL/FLG bands) (Fu & Liou, 1993; Gu et al., 2006), and a Rapid Radiative Transfer Model (RRTM) band type with 14 bands (referred to as RRTM bands) (Mlawer & Clough, 1997). The detailed band information has been provided in the supporting information (Tables S2–S4). For the broadband type with three bands (i.e., UV, visible, and NIR), we separate UV and visible bands at 0.3 μm in order to have a visible band (0.3–0.7 μm) consistent with those used in climate models (e.g., CLM) and previous studies (e.g., Dang et al., 2015). Also, the UV band (0.2–0.3 μm) has negligible solar radiation reaching the surface.

For the parameterization, we follow He, Takano, Liou, Yang, et al. (2017) to define a snow effective radius ($R_e$, see Table S1) using the specific projected area (i.e., ratio of projected area to mass) as follows:

$$R_e = \frac{3}{4\rho_i \gamma} \tag{2}$$

$$\gamma = \frac{A_{\text{snow}}}{\rho_i V_{\text{snow}}} \tag{3}$$

or equivalently,

$$R_e = \frac{3V_{\text{snow}}}{4A_{\text{snow}}} \tag{4}$$

where $\rho_i$ is the pure ice density, $V_{\text{snow}}$ is the snow grain volume, $A_{\text{snow}}$ is the snow grain projected area averaged over all directions, and $\gamma$ is the specific projected area, which is a fundamental property controlling absorption efficiency of nonspherical particles (Mitchell et al., 1996). This definition of effective size (radius of specific-projected-area-equivalent sphere) has been widely used in ice crystal modeling (Foot, 1988; Fu et al., 1999; Liou & Yang, 2016) and remote sensing retrievals (Jin et al., 2008; Zege et al., 2008).

Compared with radii of projected-area-equivalent ($R_p$) or volume-equivalent ($R_v$) spheres, we have $R_e \le R_v \le R_p$ (Fu et al., 1999). Furthermore, $R_e$ defined in this study can be quantitatively related to another commonly defined effective size ($R_{\text{SSA}} = 3/(\rho_i \beta)$, see Table S1) using the specific surface area $\beta$ (ratio of surface area to mass) (e.g., Dang et al., 2015, Flanner et al., 2007). He, Takano, Liou, Yang, et al. (2017) found that $R_{\text{SSA}} = R_e$ for sphere, hexagonal plate, and spheroid, since the surface area is 4 times larger than the projected area averaged over all directions for these convex shapes. However, the complex concave shape of Koch snowflake significantly increases its surface area and hence reduces $R_{\text{SSA}}$, leading to $R_{\text{SSA}} = 0.544R_e$ (He, Takano, Liou, Yang, et al., 2017). The relationship between $R_{\text{SSA}}$ and $R_e$ allows the application of the present parameterizations to climate models that use $R_{\text{SSA}}$.

## 3. Results and Discussions

### 3.1. Pure Snow Albedo Affected by Grain Shape

The effect of grain size on snow albedo has been well documented in the literature (e.g., Aoki et al., 2003, Warren, 1982, Wiscombe & Warren, 1980). Thus, the present study focuses on snow shape effects. Figure 1 shows the spectral albedo of fresh ($R_v$ = 100 μm) and aged ($R_v$ = 1,000 μm) pure snow for spheres, Koch snowflakes, spheroids, and hexagonal plates. Albedos of spheres and spheroids are very close (differences $<$0.005) at wavelengths $<$2.8 μm, as a result of the offsetting effects from smaller asymmetry factors and larger single-scattering coalbedos for spheroids relative to spheres (He, Takano, Liou, Yang, et al., 2017). Koch snowflakes show the highest albedo at wavelengths $<$2.8 μm primarily because of small asymmetry factors (He, Takano, Liou, Yang, et al., 2017), followed by hexagonal plates, while spheres and spheroids have the lowest albedo. The largest albedo differences among these shapes reach up to 0.15 at wavelengths of 1–1.4 μm and 1.6–2.6 μm, which, however, become very small for aged snow at 1.6–2.6 μm (Figure 1). We find that snow

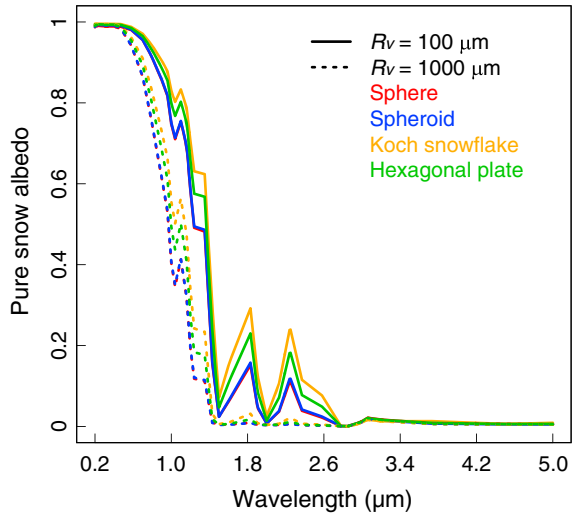


**Figure 1.** Spectral pure snow albedo from theoretical calculations for sphere (red), Koch snowflake (orange), spheroid (blue), and hexagonal plate (green) with volume-equivalent sphere radii ($R_v$) of 100 μm (solid lines) and 1,000 μm (dotted lines). Note that blue lines are overlapped with red lines due to close values.

albedo is insensitive to grain shape and size at wavelengths >2.8 μm, due to the strong snow absorption (and hence low albedo).

Dang et al. (2015) parameterized pure snow albedo as a function of effective size by assuming snow spheres. Following their empirical formulation, we develop an albedo parameterization for optically thick snow to include both spherical and nonspherical snow grains using the effective size ($R_e$ defined in equation (2)) as follows:

$$\alpha_s = b_0 + b_1 \times R_n + b_2 \times R_n^2 \quad (5)$$

$$R_n = \log_{10}(R_e/R_0) \quad (6)$$

where $\alpha_s$ is the snow albedo, $R_0$ (= 100 μm) is the reference grain effective radius, and $b_i$ ($i$ = 0–2) is the parameterization coefficient affected by snow shape and wavelength. $R_e$ in equation (6) has a unit of micrometer. Table 1 shows the broadband parameterization coefficients ($b_i$ in equation (5)) at UV (0.2–0.3 μm), visible (0.3–0.7 μm), and NIR (0.7–4.0 μm) bands. Figure 2 indicates that the parameterized results closely match with the "exact" theoretical calculations for different snow shapes at these three bands, with a normalized mean bias (NMB) close to 0, a $R^2$ of 0.9999, and a root-mean-square error (RMSE) of 0.0004 (Figure 3a). To aim at wider applications, we also provide the parameterization coefficients for the CLM bands (Table S2), FL/FLG bands (Table S3), and RRTM bands (Table S4), with very high parameterization accuracies (Figures S2–S5).

Compared with the parameterization for snow spheres developed by Dang et al. (2015), the present results are slightly lower by <0.5% and <2.5% for visible and NIR bands, respectively, due to the use of different radiative transfer models and incident solar spectra. We find that the broadband albedo difference in conjunction with shape effects increases with grain size at visible and NIR bands (Figure 2). The snow visible and NIR albedos are higher for Koch snowflakes than spheres by 0.007 and 0.043 for an effective radii ($R_e$) of 100 μm, respectively, and by 0.013 and 0.055 for $R_e$ = 1,000 μm. The difference at the NIR band mainly results from wavelengths of 0.7–1.5 μm (Figure S2). Thus, the present results suggest that snow albedo could be underestimated by more than 0.01 and 0.05 at visible and NIR bands, respectively, when snow spheres with the same effective radii are assumed instead of more realistic nonspherical grains. The grain nonsphericity effect can be even larger if considering the same snow volume/mass (equivalently $R_v$) rather than effective size ($R_e$) (see section 3.4). Wang et al. (2017) found that the spectrally (0.4–1.4 μm) averaged albedos of spherical snow grains are lower than those of hexagonal plates and fractal grains by 0.008 and 0.017, respectively, based on the AART theory (Kokhanovsky & Zege, 2004). Dang et al. (2016) quantified that if

**Table 1**
*Broadband Coefficients for the Parameterization (Equations (5) and (6)) of Pure Snow Albedo With Different Grain Shapes*

| Snow grain shape | Wavelength bands (μm) | $b_0$ | $b_1$ | $b_2$ |
|---|---|---|---|---|
| Sphere | 0.2–0.3 | 9.89547E-01 | 4.87194E-05 | −1.09677E-03 |
| | 0.3–0.7 | 9.80508E-01 | −1.36104E-02 | −1.95416E-02 |
| | 0.7–4.0 | 6.44881E-01 | −1.84202E-01 | −2.64706E-02 |
| Koch snowflake | 0.2–0.3 | 9.95458E-01 | −2.50167E-04 | −1.13382E-03 |
| | 0.3–0.7 | 9.87015E-01 | −1.34250E-02 | −1.33287E-02 |
| | 0.7–4.0 | 6.87695E-01 | −1.72401E-01 | −2.65446E-02 |
| Spheroid | 0.2–0.3 | 9.92066E-01 | 2.76519E-04 | −1.63098E-03 |
| | 0.3–0.7 | 9.81658E-01 | −1.56109E-02 | −1.93986E-02 |
| | 0.7–4.0 | 6.41406E-01 | −1.88446E-01 | −2.47061E-02 |
| Hexagonal plate | 0.2–0.3 | 9.93774E-01 | −1.94799E-04 | −1.13673E-03 |
| | 0.3–0.7 | 9.84617E-01 | −1.44812E-02 | −1.56859E-02 |
| | 0.7–4.0 | 6.66866E-01 | −1.77890E-01 | −2.75902E-02 |

*Note.* See the supporting information for other types of wavelength bands.

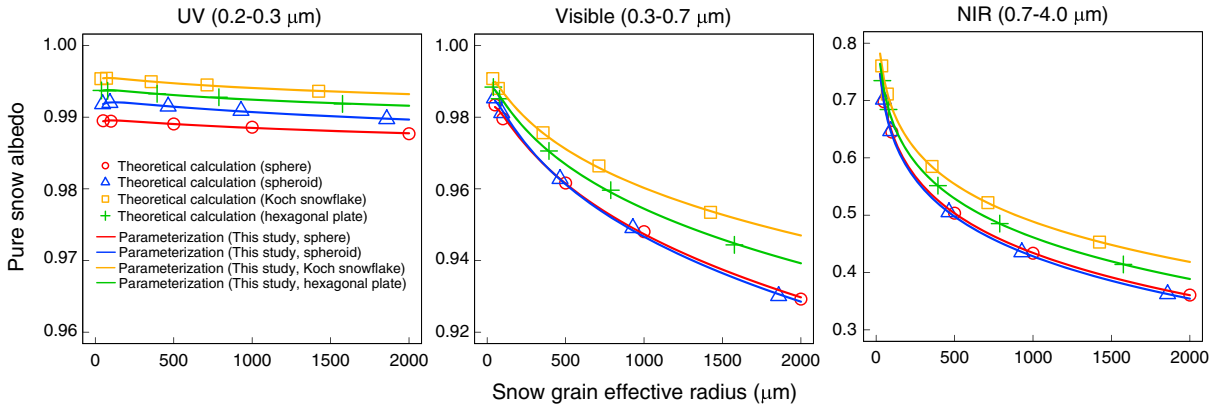


**Figure 2.** Broadband pure snow albedo as a function of snow effective radius ($R_e$ defined in equation (2)) from theoretical calculations (points) and the parameterization (equations (5) and (6)) developed in this study (solid lines) at ultraviolet (UV, 0.2–0.3 μm), visible (0.3–0.7 μm), and near-infrared (NIR, 0.7–4.0 μm) bands for sphere (red), Koch snowflake (orange), spheroid (blue), and hexagonal plate (green).

nonspherical grains are modeled as spheres, their effective radii need to be scaled down by a factor of 1.2–2.5 to achieve the correct albedo, depending on grain shape, size, and wavelength. The present results show scaling factors of 1.9–2.2 (1.7–1.8) for Koch snowflakes and 1.4–1.7 (1.3–1.4) for hexagonal plates at visible (NIR) bands. Therefore, it is important to account for nonspherical snow shapes in climate modeling. Observations (e.g., Dominé et al., 2003, Erbe et al., 2003) suggest that Koch snowflakes and spheroids could be used to mimic fresh and aged snow, respectively.

### 3.2. BC-Induced Snow Albedo Reduction

The effect of BC-snow external mixing on snow albedo has been investigated in details by previous studies (e.g., Dang et al., 2016, Flanner et al., 2007, Wiscombe & Warren, 1980). In this work, we focus on investigating the impact of BC-snow internal mixing and the resulting differences between internal and external mixing on snow albedo reduction (see section 3.3). Figure 4 shows the spectral snow albedo reduction caused by multiple BC-snow internal mixing for spherical grains, Koch snowflakes, and spheroids. We do not show results for hexagonal plates, since the BC-induced albedo reduction is very close (differences $<0.002$) to that for Koch snowflakes (Liou et al., 2014). The major albedo reductions are at UV and visible wavelengths, regardless of snow shape, size, and BC content, with much smaller reductions at 0.7–1.5 μm and negligible BC effects at wavelengths $>1.5$ μm (Figure 4), because of the strong absorption by pure snow at NIR wavelengths

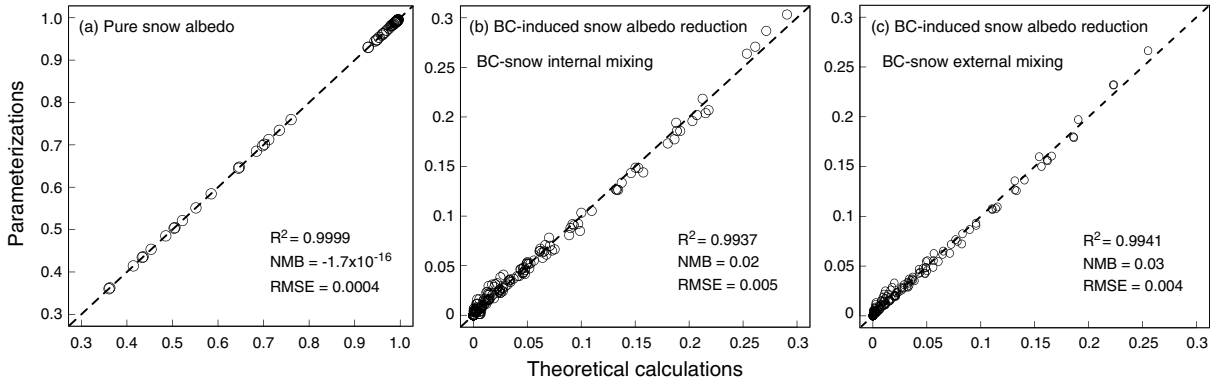


**Figure 3.** (a) Comparisons of broadband pure snow albedo at ultraviolet (UV, 0.2–0.3 μm), visible (0.3–0.7 μm), and near-infrared (NIR, 0.7–4.0 μm) bands from theoretical calculations and the parameterization (equations (5) and (6)) developed in this study for sphere, Koch snowflake, spheroid, and hexagonal plate with different sizes (see Table S1 for details). (b) Comparisons of broadband BC-induced snow albedo reduction at UV, visible, and NIR bands from theoretical calculations and the parameterization (equations (7) and (8)) developed in this study for sphere, Koch snowflake, and spheroid internally mixed with different BC contents (see Table S1 for details). (c) Same as Figure 3b but for BC-snow external mixing. Also shown in all panels are the normalized mean bias (NMB), root-mean-square error (RMSE), and coefficient of determination ($R^2$) for the parameterizations. The dashed lines are 1:1 ratio lines.

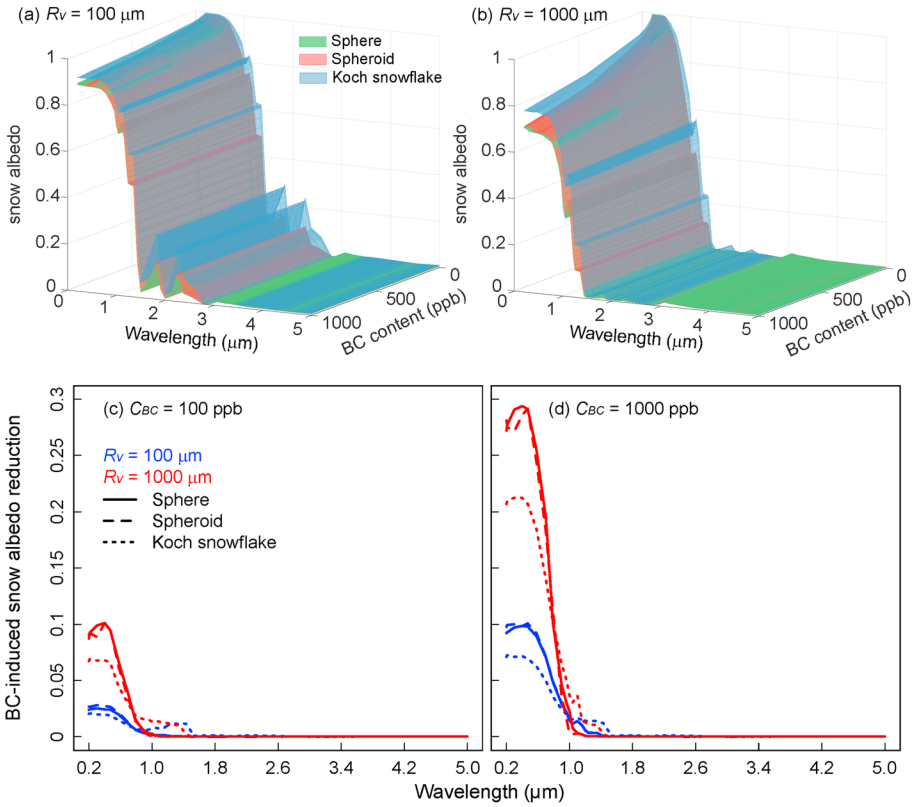


**Figure 4.** Snow albedo from theoretical calculations as a function of wavelength and BC content in snow for sphere (green), Koch snowflake (blue), and spheroid (red) with volume-equivalent sphere radii ($R_v$) of (a) 100 μm and (b) 1,000 μm. Spectral BC-induced snow albedo reduction from theoretical calculations for BC contents ($C_{BC}$) of (c) 100 ppb and (d) 1,000 ppb internally mixed within snow sphere (solid line), Koch snowflake (dotted line), and spheroid (dashed line) with volume-equivalent sphere radii ($R_v$) of 100 μm (blue) and 1,000 μm (red).

(Warren & Wiscombe, 1980). We find that spheres and spheroids show similar spectral albedo reductions for different BC concentrations and snow sizes (Figure 4). The BC-induced albedo reduction for Koch snowflakes is much smaller than that for spheres by up to ~0.1 at UV and visible wavelengths (Figures 4c–4d) as a result of smaller asymmetry factors and hence less forward scattering for Koch snowflakes (He, Takano, Liou, Yang, et al., 2017). The larger extinction coefficients for Koch snowflakes also contribute to the smaller BC-induced albedo reduction when using the same $R_v$ (or grain volume) instead of $R_e$ (see section 3.4).

Following the empirical formulation proposed by Hadley and Kirchstetter (2012) based on laboratory measurements, we further develop a parameterization of albedo reduction ($\Delta\alpha_s$) caused by BC-snow internal mixing for optically thick snow with different grain shapes as follows:

$$\Delta\alpha_s = d_0 \times (C_{BC})^k \tag{7}$$

$$k = d_1 \times (R_e/R_0)^{d_2} \tag{8}$$

where $C_{BC}$ (in units of ppb) is the BC mass content in snow, $R_0$ (= 100 μm) is the reference snow effective radius, $R_e$ (unit: μm) is the snow effective radius defined in equation (2), and $d_i$ ($i$ = 0–2) is the parameterization coefficient as a function of snow shape and wavelength. Table 2 shows the broadband parameterization coefficients ($d_i$ in equations (7) and (8)) at UV (0.2–0.3 μm), visible (0.3–0.7 μm), and NIR (0.7–4.0 μm) bands. We find that the parameterized results fit closely with the "exact" theoretical calculations for different snow shapes at these three bands (Figure 5), with a NMB of 0.02, a $R^2$ of 0.994, and a RMSE of 0.005 (Figure 3b). For a broader application, we also provide the parameterization coefficients for the CLM bands (Table S5), FL/FLG bands (Table S6), and RRTM bands (Table S7), with very high parameterization accuracies (Figures S6–S9). To enhance applicability to climate and land surface models, we further extend the present parameterization

**Table 2**
*Broadband Coefficients for the Parameterizations (Equations (7) and (8)) of Snow Albedo Reductions Caused by BC-Snow Internal and External Mixing*

| Snow grain shape[a] | Wavelength bands (μm) | $d_0$ | $d_1$ | $d_2$ |
|---|---|---|---|---|
| | | *BC-Snow Internal Mixing* | | |
| Sphere | 0.2–0.3 | 6.67899E-03 | 3.79850E-01 | 1.62639E-01 |
| | 0.3–0.7 | 4.00225E-03 | 4.47263E-01 | 1.34864E-01 |
| | 0.7–4.0 | 1.59399E-04 | 7.38319E-01 | 5.60124E-02 |
| Koch snowflake | 0.2–0.3 | 4.79623E-03 | 4.08959E-01 | 1.53431E-01 |
| | 0.3–0.7 | 2.80587E-03 | 4.72359E-01 | 1.33016E-01 |
| | 0.7–4.0 | 1.29313E-03 | 4.28793E-01 | 1.13120E-01 |
| Spheroid | 0.2–0.3 | 6.41487E-03 | 4.06470E-01 | 1.35791E-01 |
| | 0.3–0.7 | 4.00213E-03 | 4.57966E-01 | 1.25910E-01 |
| | 0.7–4.0 | 1.48671E-04 | 7.46812E-01 | 5.15241E-02 |
| | | *BC-Snow External Mixing* | | |
| Sphere | 0.2–0.3 | 5.31081E-03 | 3.96987E-01 | 1.54618E-01 |
| | 0.3–0.7 | 3.01470E-03 | 4.68312E-01 | 1.27961E-01 |
| | 0.7–4.0 | 1.10568E-04 | 7.53732E-01 | 6.62209E-02 |
| Koch snowflake | 0.2–0.3 | 3.09660E-03 | 4.20585E-01 | 1.55643E-01 |
| | 0.3–0.7 | 1.57041E-03 | 5.02587E-01 | 1.27417E-01 |
| | 0.7–4.0 | 5.03177E-05 | 7.92972E-01 | 7.16926E-02 |
| Spheroid | 0.2–0.3 | 4.61057E-03 | 4.01980E-01 | 1.54512E-01 |
| | 0.3–0.7 | 2.39483E-03 | 4.82428E-01 | 1.25756E-01 |
| | 0.7–4.0 | 7.33963E-05 | 7.78737E-01 | 6.55470E-02 |

*Note.* See supporting information for other types of wavelength bands.
[a]We do not parameterize for hexagonal plate, since its BC-induced albedo reduction is very close to that for Koch snowflake.

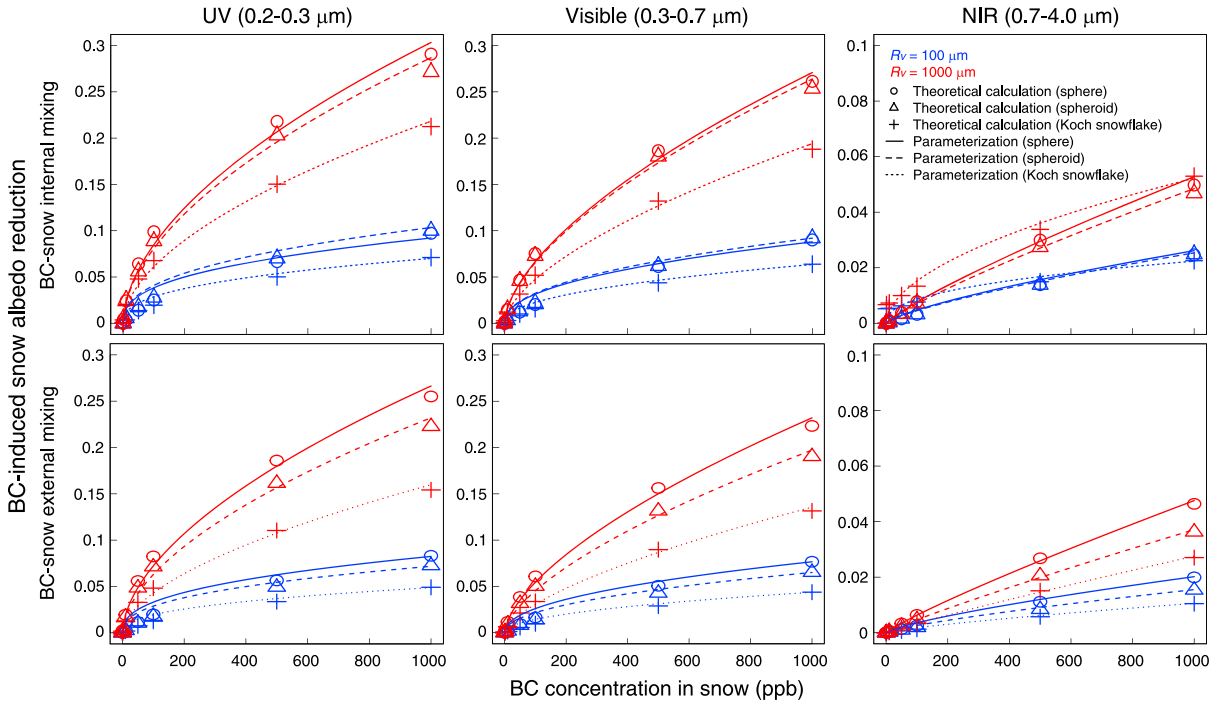


**Figure 5.** Broadband BC-induced snow albedo reduction for BC-snow (top row) internal and (bottom row) external mixing as a function of BC concentration from theoretical calculations (points) and the parameterization (equations (7) and (8)) developed in this study (lines) at (left column) ultraviolet (UV, 0.2–0.3 μm), (middle column) visible (0.3–0.7 μm), and (right column) near-infrared (NIR, 0.7–4.0 μm) bands for sphere (circle and solid line), Koch snowflake (cross and dotted line), and spheroid (triangle and dashed line) with volume-equivalent sphere radii ($R_v$) of 100 μm (blue) and 1,000 μm (red).

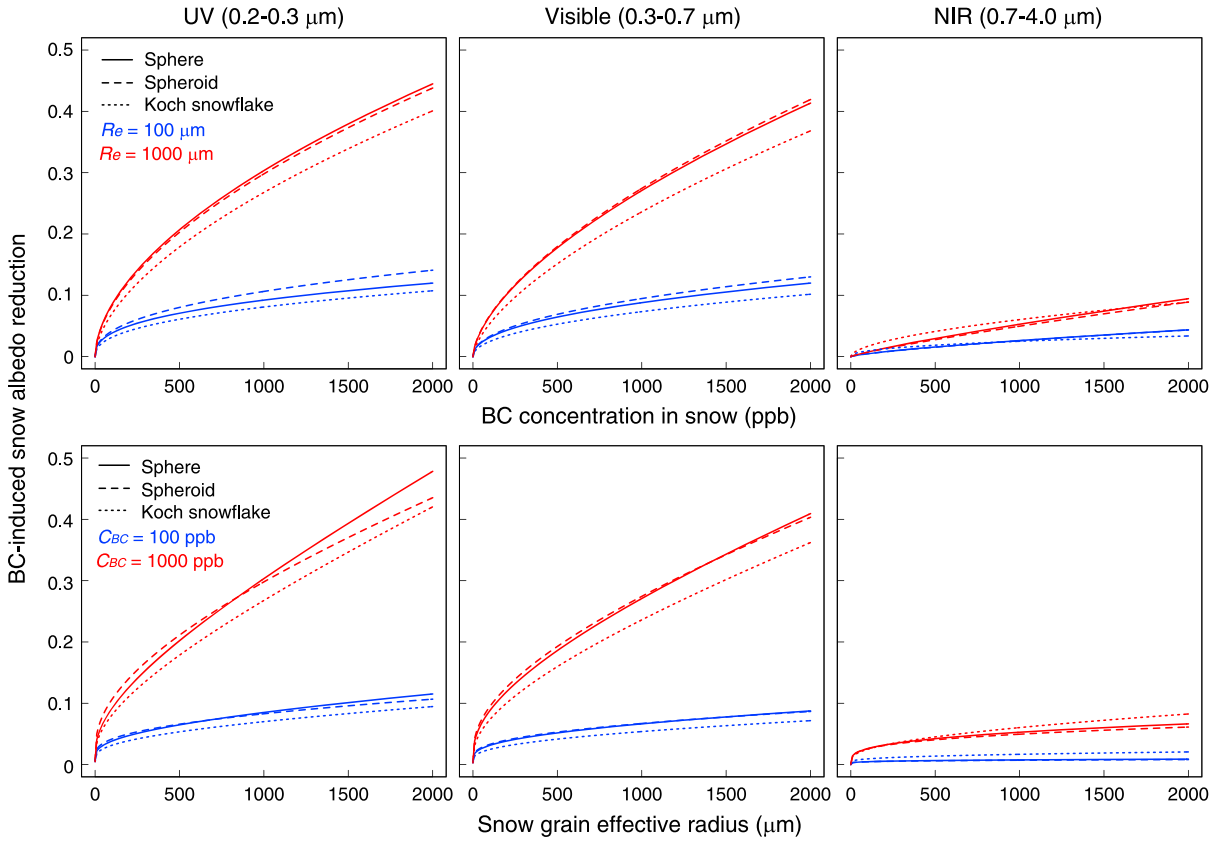


**Figure 6.** (top row) Broadband BC-induced snow albedo reduction as a function of BC concentration internally mixed in snow ($C_{BC}$) from the parameterization (equations (7) and (8)) developed in this study at (left column) ultraviolet (UV), (middle column) visible, and (right column) near-infrared (NIR) bands for sphere (solid line), Koch snowflake (dotted line), and spheroid (dashed line) with snow effective radii ($R_e$ defined in equation (2)) of 100 μm (blue) and 1,000 μm (red). (bottom row) Same as Figure 6 (top row) but for BC-induced snow albedo reduction as a function of snow effective radius ($R_e$) with $C_{BC}$ of 100 ppb (blue) and 1,000 ppb (red). See Figure S10 for the results of BC-snow external mixing.

(equations (7) and (8)) to include BC-snow external mixing scenarios with very high accuracies (Figures 3c and S6–S9). We have provided the parameterization coefficients in Tables 2 and S8–S10 for the different types of wavelength bands. Note that we do not show results for wavelengths >1.5 μm, due to negligible BC effects on snow albedo at these wavelengths.

Figure 6 shows the broadband snow albedo reduction caused by BC-snow internal mixing as a function of BC content or snow effective radius ($R_e$) for different snow shapes based on the parameterization (equations (7) and (8)). The albedo reductions at UV and visible bands are a factor of 2–10 stronger than that at the NIR band, depending on snow size and BC content (Figure 6). The broadband albedo reductions are very close (relative differences <5%) for spheroids and spheres, except for a 10–20% difference under very high BC contents (>1,000 ppb) at the UV band, where the incident solar energy is rather small. Koch snowflakes consistently show less broadband albedo reductions than spheres at UV and visible wavelengths by up to 0.06 (or 30% in relative difference), whereas they display slightly (<0.016) stronger reductions at the NIR band for very large sizes ($R_e$ > 1,000 μm). For 100 ppb BC in snow, we find that visible albedo reductions are smaller for Koch snowflakes than spheres by 0.007 and 0.013 for fresh ($R_e$ = 100 μm) and aged ($R_e$ = 1,000 μm) snow, respectively. Thus, considering the nature of grain nonsphericity, assuming spherical snow grains with the same effective sizes, may cause nontrivial biases in determining BC-induced snow albedo reduction. He et al. (2014) found that Koch snowflakes decrease BC-induced albedo reduction by 20–40% in comparison with spherical counterparts for BC-snow internal mixing. Moreover, the difference in albedo reductions among different shapes varies with grain size and BC concentration (Figure 6), implying that snow shape effects could be spatiotemporally heterogeneous. We note that the impact of grain nonsphericity on BC-contaminated snow albedo is further enlarged with the same $R_v$ rather than $R_e$ (see section 3.4).

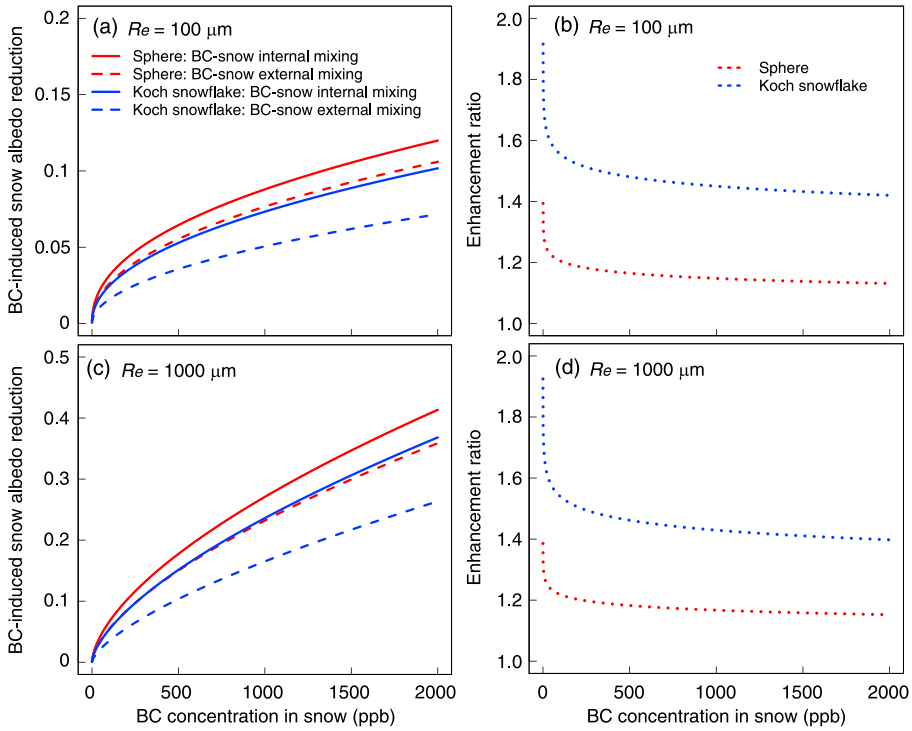


**Figure 7.** (a) BC-induced snow albedo reduction as a function of BC concentration in snow at the visible band (0.3–0.7 μm) for sphere (red) and Koch snowflake (blue) with BC-snow internal (solid line) and external (dashed line) mixing with a snow effective radius ($R_e$ defined in equation (2)) of 100 μm. (b) The enhancement due to internal mixing relative to external mixing for the BC-induced snow albedo reduction with an $R_e$ of 100 μm shown in Figure 7a. (c) Same as Figure 7a but for an $R_e$ of 1,000 μm. (d) Same as Figure 7b but for an $R_e$ of 1,000 μm.

### 3.3. Effects of Multiple BC-Snow Internal Mixing

Figure 7 shows the snow albedo reduction caused by BC-snow internal and external mixing for spheres and Koch snowflakes with $R_e$ of 100 and 1,000 μm at the visible band (0.3–0.7 μm). Compared with external mixing, multiple BC-snow internal mixing enhances albedo reduction by a factor of 1.2–1.4 and 1.4–2.0 for spheres and Koch snowflakes, respectively, depending on BC content. For example, 100 ppb BC in fresh snow ($R_e$ = 100 μm) leads to albedo reductions of 0.031 and 0.025 for internal mixing in the cases of spheres and Koch snowflakes, respectively, while the reductions are 0.026 and 0.016 for external mixing counterparts. The enhancement from BC-snow internal mixing slightly decreases as snow size increases (Figures 7b and 7d; see also Flanner et al., 2012). In addition, the effect of snow grain nonsphericity for external mixing is stronger than that for internal mixing (Figures 7a and 7c). We further note that Koch snowflakes internally mixed with BC have albedo reductions similar to those for spheres externally mixed with BC (Figures 7a and 7c), revealing that snow nonsphericity effects may offset the effects of multiple internal mixing under certain circumstances (Figure S11). Thus, it is imperative to assess the uncertainty associated with snow grain shape and BC-snow mixing state simultaneously (see section 4).

Moreover, the enhancement due to multiple BC-snow internal mixing is much larger for BC contents of $<$200 ppb than higher contents (Figures 7b and 7d). This suggests that BC-snow mixing state is particularly important for regions with relatively low BC concentrations. Observations have shown that the majority of Northern Hemispheric snowpack has BC concentrations of $<$200 ppb (Qian et al., 2015), where BC-snow internal mixing can lead to a factor of up to 1.4 (2.0) stronger albedo reductions for spheres (Koch snowflakes) relative to external mixing. However, the highly polluted northeastern China has BC contents of $>$1,000 ppb (Wang et al., 2013), where internal mixing enhances albedo reductions by about 20% and 40% for spheres and Koch snowflakes, respectively.

To date, only very few studies have explicitly accounted for BC-snow internal mixing. Flanner et al. (2012) found a 43–86% higher BC-induced global land snow albedo forcing for combined BC-snow internal and

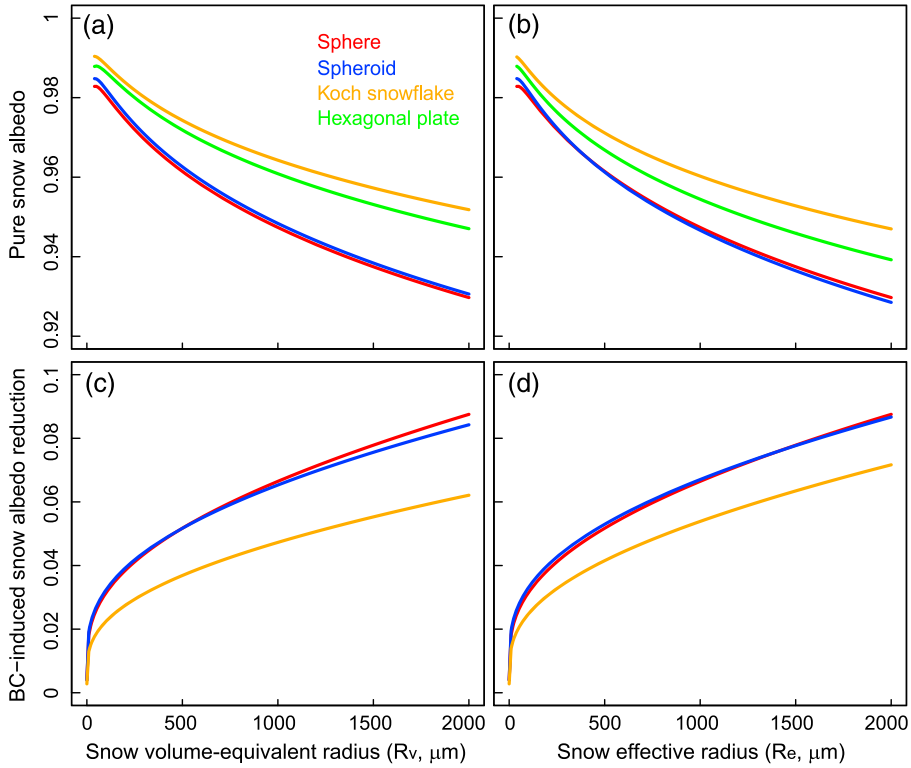


**Figure 8.** (a, b) Pure snow albedo and (c, d) BC-induced albedo reduction (with 100 ppb BC internally mixed with snow) at the visible band (0.3–0.7 μm) as a function of (a, c) snow volume-equivalent radius ($R_v$) and (b, d) snow effective radius ($R_e$ defined in equation (2)) for sphere (red), spheroid (blue), Koch snowflake (orange), and hexagonal plate (green). Note that values for hexagonal plates are not shown in Figures 8c and 8d, owing to very close BC-induced albedo reductions between hexagonal plates and Koch snowflakes. See text for details.

external mixing than that for purely external mixing by assuming spherical snow grains. Liou et al. (2014) pointed out that BC-snow internal mixing has different impacts on Koch snowflakes and spherical grains. He et al. (2014) showed that the BC-induced albedo forcing for Koch snowflakes over global land snowpack is increased by 40–60% due to internal mixing relative to external mixing. Wang et al. (2017) found that internal mixing further lower snow albedo by 0.005 for 100 ppb BC and 0.036 for 3000 ppb BC for hexagonal grains compared with external mixing.

### 3.4. Effects of Snow Volume Equivalent and Effective Radii

There are two measures of snow grain sizes used in this study, the volume-equivalent radius ($R_v$) and the effective radius ($R_e$ defined in equation (2)). We used $R_v$ to construct different snow shapes with the same grain volume and conducted albedo calculations to generate a data set for parameterization, and at the same time, we used $R_e$ as a key parameter in albedo parameterizations. We note that the shape effects on snow albedo and BC-induced albedo reduction are enlarged under the same $R_v$ compared with the same $R_e$. For example, when assuming the same $R_v$, the differences between spheres and Koch snowflakes in pure snow albedo and BC-induced albedo reduction at the visible band increase by 10–30% and 20–60%, respectively, in comparison to assuming the same $R_e$ (Figure 8). This is because nonspherical snow grains have a smaller $R_e$ than spheres under the same $R_v$ (or grain volume) (see also Table S1). As a result, a smaller $R_e$ of nonspherical grains leads to a smaller snow single-scattering coalbedo and a larger snow extinction coefficient. For pure snow, a smaller single-scattering coalbedo (compared to the case with the same $R_e$) results in a higher snow albedo for nonspherical grains (Figures 8a and 8b), which reinforces the effect of a smaller asymmetry factor (see section 3.1), while a larger snow extinction coefficient makes negligible contributions due to the assumption of optically semi-infinite snow layers. Thus, the difference in pure snow albedo between nonspherical and spherical grains is larger under the same $R_v$ than that under the same $R_e$. For BC-contaminated snow

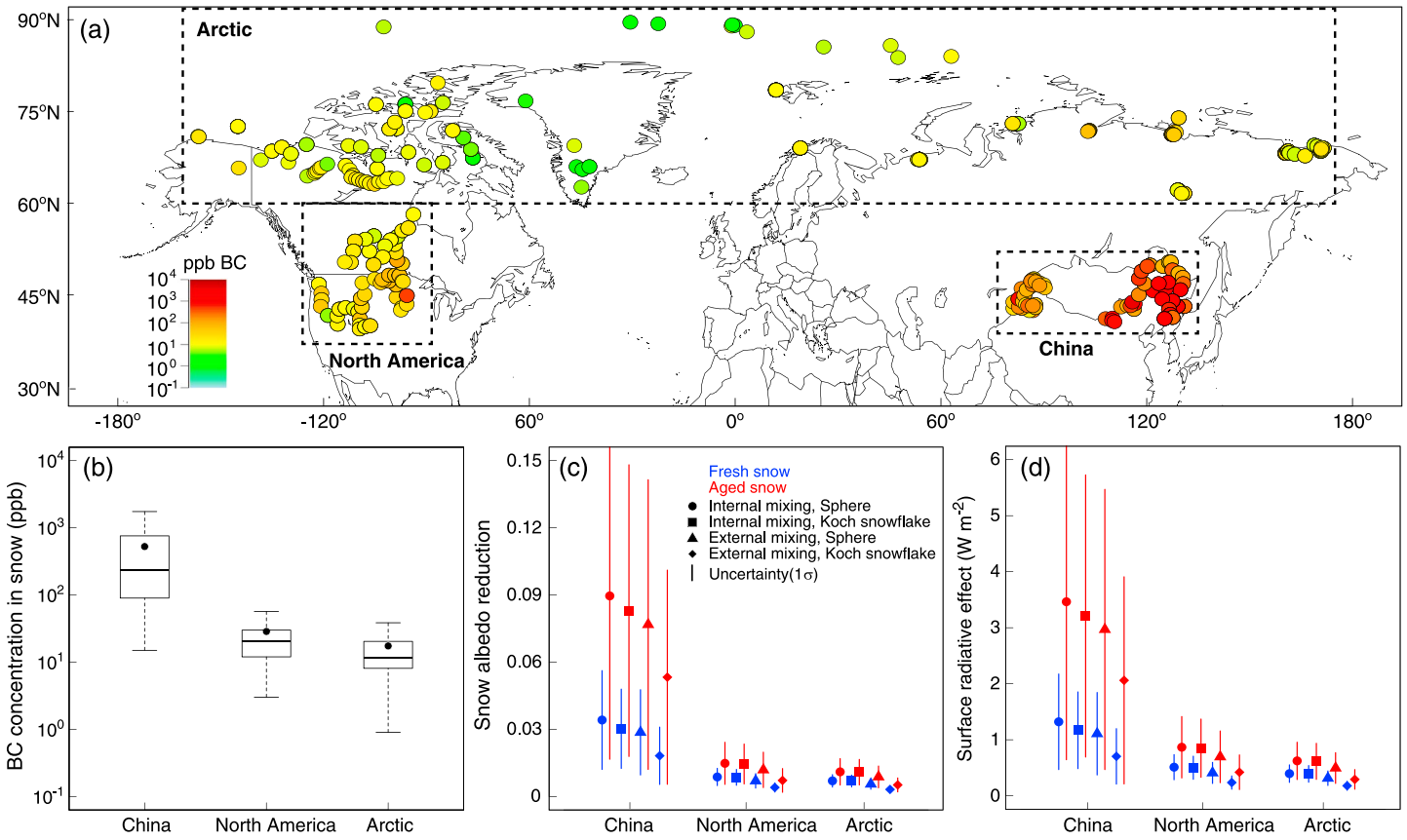


**Figure 9.** (a) Spatial distributions of observed BC concentrations in snow over China, North America, and the Arctic through January to May during 2007–2013. See text for details. (b) Regional mean (solid dots), median (bold bar), interquartile range (i.e., between 25th and 75th percentiles; box), and maximum/minimum (whiskers) within ±1.5 times interquartile range for BC concentrations in snow over China, North America, and the Arctic. (c) Snow albedo reductions (integrated through 0.2–5.0 μm wavelengths) caused by observed BC concentrations shown in Figure 9b for fresh (blue, $R_e$ = 100 μm) and aged (red, $R_e$ = 1,000 μm) snow with BC-snow internal mixing for spheres (circles) and Koch snowflakes (squares) as well as BC-snow external mixing for spheres (triangles) and Koch snowflakes (diamonds). Also shown is one standard deviation (1$\sigma$) uncertainty (vertical lines) due to the variability of BC concentrations within each region. (d) Same as Figure 9c but for surface radiative effects caused by BC-induced snow albedo reductions shown in Figure 9c. In the calculations, we assume that the ground surface is covered by thick snow with no canopy based on the snow cover fraction obtained from MERRA-2. See Figure S12 for overall variations of albedo reductions and radiative effects caused by snow shape, BC-snow mixing state, and BC content in snow over the three regions.

with the same $R_v$, both the larger snow extinction coefficient and the smaller asymmetry factor of nonspherical grains reduce the penetration depth of solar radiation into snow and hence BC absorption in snow, while in the case of snow with the same $R_e$, only the asymmetry factor contributes to the difference between nonspherical and spherical snow grains. This leads to smaller BC-induced albedo reductions for nonspherical grains and larger differences in albedo reductions between spherical and nonspherical grains when assuming the same $R_v$ instead of the same $R_e$ (Figures 8c and 8d).

## 4. Implication for Snow Albedo Radiative Effects

To quantify surface radiative effects caused by BC contamination in real snowpack, we use a comprehensive set of BC-in-snow measurements (Figure 8a) in Northern Hemisphere based on field campaigns over the Arctic in spring of 2007–2009 (Doherty et al., 2010), North America in winter of 2013 (Doherty et al., 2014), and Northern China in winter of 2010 and 2012 (Wang et al., 2013; Ye et al., 2012), which has been summarized and presented in Qi, Li, He, et al. (2017) and Qi, Li, Li, et al. (2017). Combining these BC observations with the present parameterizations for BC-induced albedo reduction (equations (7)–(8)), we compute the corresponding snow albedo reductions by assuming optically thick snow layers. We further derive surface radiative effects by multiplying the albedo reduction with surface downward solar radiation under the all-sky condition obtained from the Modern-Era Retrospective analysis for Research and Applications version 2

**Table 3**
*Regional Mean BC-Induced Snow Albedo Reductions and Surface Radiative Effects Based On Observed BC Concentrations in Snow*

| | | Sphere | | | | Koch snowflake | | | |
|---|---|---|---|---|---|---|---|---|---|
| | | $R_e$ = 100 μm | | $R_e$ = 1,000 μm | | $R_e$ = 100 μm | | $R_e$ = 1,000 μm | |
| Region | Observed BC content (ppb) | Internal mixing | External mixing | Internal mixing | External mixing | Internal mixing | External mixing | Internal mixing | External mixing |
| | | | | | *Snow Albedo Reduction* | | | | |
| China | 526.5 | 0.034 | 0.029 | 0.090 | 0.077 | 0.030 | 0.018 | 0.083 | 0.053 |
| North America | 28.7 | 0.009 | 0.007 | 0.015 | 0.012 | 0.008 | 0.004 | 0.014 | 0.007 |
| Arctic | 17.4 | 0.007 | 0.006 | 0.011 | 0.009 | 0.007 | 0.003 | 0.011 | 0.005 |
| | | | | | *Surface Radiative Effect (W m$^{-2}$)* | | | | |
| China | 526.5 | 1.32 | 1.11 | 3.46 | 2.97 | 1.17 | 0.70 | 3.21 | 2.06 |
| North America | 28.7 | 0.51 | 0.41 | 0.87 | 0.70 | 0.50 | 0.24 | 0.85 | 0.42 |
| Arctic | 17.4 | 0.40 | 0.31 | 0.62 | 0.49 | 0.39 | 0.18 | 0.61 | 0.29 |

(MERRA-2) reanalysis data produced by the NASA Global Modeling and Assimilation Office (https://gmao.gsfc.nasa.gov/reanalysis/MERRA-2/), assuming that no canopy covers the ground snow. The preceding assumptions could lead to an overestimate of BC radiative effects if the regions were largely snow free, particularly for midlatitude snowpack regions in late spring. To alleviate this overestimation, we multiply the surface radiative effects by the snow cover fraction from MERRA-2 and average the hourly surface radiation and snow cover fraction data over the period of BC measurements (i.e., from January to May in 2007–2013) and three individual regions (i.e., Arctic, North America, and China). To assess the uncertainty caused by combined effects of snow grain shape and BC-snow mixing state, we employ eight computation scenarios with different snow shapes (sphere or Koch snowflake) and BC-snow mixing states (internal or external) for fresh ($R_e$ = 100 μm) and aged ($R_e$ = 1,000 μm) snow.

Figure 9a shows the spatial distribution of BC-in-snow observations over China, North America, and the Arctic. Figure 9b illustrates that China snowpack has the highest regional mean BC content in snow (~500 ppb), particularly at hot spots in northeastern China, while the regional mean BC contents are much lower in the Arctic (~20 ppb) and North America (~30 ppb). Accordingly, the regional mean BC-induced snow albedo reductions are 0.029, 0.007, and 0.006 in China, North America, and the Arctic, respectively, in the case of fresh snow spheres externally mixed with BC (Figure 9c), which correspond to surface radiative effects of 1.11, 0.41, and 0.31 W m$^{-2}$ (Figure 9d). We find that aged snow increases albedo reductions and surface radiative effects by a factor of 1.5–3.0 relative to fresh snow (Figures 9c and 9d). A change in snow grain shape from spheres to Koch snowflakes leads to a decrease of 30–50% in the BC-induced albedo effects over the three regions for external BC-snow mixing but a decrease of less than 15% for internal mixing (Table 3). A change in the BC-snow mixing state from external to internal mixing leads to an increase of 15–30% in the albedo effects for snow spheres over the three regions but can reach up to 130% for Koch snowflakes in the Arctic (Table 3). The results indicate that snow shape and BC-snow mixing state could have opposite impacts on BC-induced albedo effects, so that it is necessary to use realistic shape and mixing state in climate modeling and analysis. Finally, the overall uncertainty ($1\sigma$) induced by snow shape and BC-snow mixing state is 21–32% in the aforementioned three regions.

The present estimates have limitations, which require further improvements. For example, we assume semi-infinite snow layers with no canopy and only include BC as an absorbing aerosol in snow, which could overestimate BC-induced surface radiative effects. In the calculation of regional mean values, spatial variation in the sampling density of observed BC content in snow was not accounted for, which could introduce uncertainty. Finally, for a comprehensive understanding, a coupling of dynamic snow models with climate models using realistic meteorological conditions is required.

## 5. Conclusions

We quantified the impact of snow grain shape and multiple BC-snow internal mixing on snow albedo by explicitly resolving the structures of BC-snow mixtures for spheres, Koch snowflakes, spheroids, and hexagonal plates. We further developed a set of parameterizations for pure snow albedo and BC-induced albedo

reduction to account for snow shape and BC-snow internal/external mixing for application to climate models. We then estimated BC-induced albedo reduction and surface radiative effects over the major snowpack in Northern Hemisphere as well as associated uncertainties caused by snow shape and BC-snow mixing state.

We found that Koch snowflakes had the highest albedo, followed by hexagonal plates, while spheroids and spheres with the same effective sizes ($R_e$) had the lowest albedo. The broadband albedo difference due to shape effects increased with snow grain size, with higher albedos for Koch snowflakes than spherical counterparts by 0.013 (0.055) with a $R_e$ of 1,000 μm at visible (NIR) bands. As such, snow albedo could be underestimated if spherical grains with the same effective sizes were assumed instead of more realistic nonspherical grains. We further parameterized pure snow albedo as a function of effective size for different shapes based on the "exact" theoretical calculations, with very high accuracies.

We found that multiple BC-snow internal mixing mainly led to snow albedo reductions at UV and visible wavelengths, with negligible effects at wavelengths $>$1.5 μm, while the reductions were much larger for aged snow than fresh snow. For the same effective size, spheres and spheroids showed similar BC-induced albedo reductions. However, the albedo reductions for Koch snowflakes were smaller than those for spheres by up to 0.06 at UV and visible wavelengths, depending on grain size and BC content. We further parameterized the BC-induced albedo reduction for both internal and external mixing as a function of BC content and snow effective size for different shapes with reference to the "exact" theoretical calculations, with very high accuracies.

Compared with external mixing, multiple BC-snow internal mixing enhanced snow albedo reductions by a factor of 1.2–1.4 (1.4–2.0) for spheres (Koch snowflakes), with stronger enhancements for small BC concentrations (particularly $<$200 ppb). Furthermore, the enhanced albedo reduction due to internal mixing can be offset by the weakened albedo reduction due to snow grain nonsphericity.

Combining the present parameterizations with observations of BC content in snow, we estimated regional mean BC-induced snow albedo reductions of 0.029, 0.007, and 0.006 in China, North America, and the Arctic, respectively, corresponding to surface radiative effects of 1.11, 0.41, and 0.31 W $m^{-2}$ for fresh snow spheres externally mixed with BC. Using Koch snowflakes reduced the albedo effects by up to 50%, while assuming internal rather than external mixing enhanced the albedo effects by up to 30% (130%) for spherical (nonspherical) snow grains. The overall uncertainty ($1\sigma$) caused by snow shape and BC-snow mixing state was on the order of 21–32% in the three regions.

Overall, both snow grain shape and multiple BC-snow internal mixing are key elements in resolving BC-snow interactions and associated radiative effects. The present parameterizations can be conveniently incorporated into land surface and climate models. For further study on the evaluation of BC-induced snow albedo effects under various environmental conditions, a coupling of climate models with dynamic snow models is necessary.

**Acknowledgments**
We thank all the reviewers for their constructive comments. This study was supported by NSF grant AGS-1660587. The authors thank Cheng Dang for helpful discussions. The National Center for Atmospheric Research (NCAR) is sponsored by the National Science Foundation (NSF). C. He thanks the NCAR Advanced Study Program (ASP) Fellowship sponsored by NSF. Users can access the new data produced by this study through the supplementary materials and the MERRA-2 data from the link provided in the text. The authors declare no conflicts of interest.

## References

Aoki, T., Hachikubo, A., & Hori, M. (2003). Effects of snow physical parameters on shortwave broadband albedos. *Journal of Geophysical Research*, *108*(D19), 4616. https://doi.org/10.1029/2003JD003506

Aoki, T., Kuchiki, K., Niwano, M., Kodama, Y., Hosaka, M., & Tanaka, T. (2011). Physically based snow albedo model for calculating broadband albedos and the solar heating profile in snowpack for general circulation models. *Journal of Geophysical Research*, *116*, D11114. https://doi.org/10.1029/2010JD015507

Bond, T. C., & Bergstrom, R. W. (2006). Light absorption by carbonaceous particles: An investigative review. *Aerosol Science and Technology*, *40*, 27–67. https://doi.org/10.1080/02786820500421521

Bond, T. C., Doherty, S. J., Fahey, D. W., Forster, P. M., Berntsen, T., DeAngelo, B. J., … Zender, C. S. (2013). Bounding the role of black carbon in the climate system: A scientific assessment. *Journal of Geophysical Research: Atmospheres*, *118*, 5380–5552. https://doi.org/10.1002/jgrd.50171

Dang, C., Brandt, R. E., & Warren, S. G. (2015). Parameterizations for narrowband and broadband albedo of pure snow and snow containing mineral dust and black carbon. *Journal of Geophysical Research: Atmospheres*, *120*, 5446–5468. https://doi.org/10.1002/2014JD022646

Dang, C., Fu, Q., & Warren, S. (2016). Effect of snow grain shape on snow albedo. *Journal of the Atmospheric Sciences*, *73*(9), 3573–3583. https://doi.org/10.1175/JAS-D-15-0276.1

Dang, C., Warren, S. G., Fu, Q., Doherty, S. J., & Sturm, M. (2017). Measurements of light-absorbing particles in snow across the Arctic, North America, and China: Effects on surface albedo. *Journal of Geophysical Research: Atmospheres*, *122*, 10,149–10,168. https://doi.org/10.1002/2017JD027070

Doherty, S. J., Dang, C., Hegg, D. A., Zhang, R., & Warren, S. G. (2014). Black carbon and other light-absorbing particles in snow of central North America. *Journal of Geophysical Research: Atmospheres*, *119*, 12,807–12,831. https://doi.org/10.1002/2014JD022350

Doherty, S. J., Warren, S. G., Grenfell, T. C., Clarke, A. D., & Brandt, R. E. (2010). Light-absorbing impurities in Arctic snow. *Atmospheric Chemistry and Physics*, *10*, 11,647–11,680. https://doi.org/10.5194/acp-10-11647-2010

Dominé, F., Lauzier, T., Cabanes, A., Legagneux, L., Kuhs, W. F., Techmer, K., & Heinrichs, T. (2003). Snow metamorphism as revealed by scanning electron microscopy. *Microscopy Research and Technique*, *62*(1), 33–48. https://doi.org/10.1002/jemt.10384

Erbe, E. F., Rango, A., Foster, J., Josberger, E. G., Pooley, C., & Wergin, W. (2003). Collecting, shipping, storing, and imaging snow crystals and ice grains with low-temperature scanning electron microscopy. *Microscopy Research and Technique*, *62*(1), 19–32. https://doi.org/10.1002/jemt.10383

Flanner, M. G., Liu, X., Zhou, C., Penner, J. E., & Jiao, C. (2012). Enhanced solar energy absorption by internally-mixed black carbon in snow grains. *Atmospheric Chemistry and Physics*, *12*, 4699–4721. https://doi.org/10.5194/acp-12-4699-2012

Flanner, M. G., Zender, C. S., Randerson, J. T., & Rasch, P. J. (2007). Present-day climate forcing and response from black carbon in snow. *Journal of Geophysical Research*, *112*, D11202. https://doi.org/10.1029/2006JD008003

Foot, J. S. (1988). Some observations of the optical properties of clouds: II. Cirrus. *Quarterly Journal of the Royal Meteorological Society*, *114*(479), 145–164. https://doi.org/10.1002/qj.49711447908

Fu, Q. (2007). A new parameterization of an asymmetry factor of cirrus clouds for climate models. *Journal of the Atmospheric Sciences*, *64*, 4140–4150. https://doi.org/10.1175/2007JAS2289.1

Fu, Q., & Liou, K. N. (1993). Parameterization of the radiative properties of cirrus clouds. *Journal of the Atmospheric Sciences*, *50*(13), 2008–2025. https://doi.org/10.1175/1520-0469(1993)050%3C2008:POTRPO%3E2.0.CO;2

Fu, Q., Sun, W. B., & Yang, P. (1999). Modeling of scattering and absorption by nonspherical cirrus ice particles at thermal infrared wavelengths. *Journal of the Atmospheric Sciences*, *56*(16), 2937–2947. https://doi.org/10.1175/1520-0469(1999)056%3C2937:MOSAAB%3E2.0.CO;2

Gardner, A. S., & Sharp, M. J. (2010). A review of snow and ice albedo and the development of a new physically based broadband albedo parameterization. *Journal of Geophysical Research*, *115*, F01009. https://doi.org/10.1029/2009JF001444

Gu, Y., Liou, K. N., Xue, Y., Mechoso, C. R., Li, W., & Luo, Y. (2006). Climatic effects of different aerosol types in China simulated by the UCLA general circulation model. *Journal of Geophysical Research*, *111*, D15201. https://doi.org/10.1029/2005JD006312

Hadley, O. L., & Kirchstetter, T. W. (2012). Black-carbon reduction of snow albedo. *Nature Climate Change*, *2*, 437–440. https://doi.org/10.1038/nclimate1433

Hansen, J. E., & Nazarenko, L. (2004). Soot climate forcing via snow and ice albedos. *Proceedings of the National Academy of Sciences of the United States of America*, *101*, 423–428. https://doi.org/10.1073/pnas.2237157100

He, C., Li, Q., Liou, K.-N., Takano, Y., Gu, Y., Qi, L., … Leung, L. R. (2014). Black carbon radiative forcing over the Tibetan Plateau. *Geophysical Research Letters*, *41*, 7806–7813. https://doi.org/10.1002/2014GL062191

He, C., Liou, K. N., Takano, Y., Zhang, R., Levy Zamora, M., Yang, P., … Leung, L. R. (2015). Variation of the radiative properties during black carbon aging: Theoretical and experimental intercomparison. *Atmospheric Chemistry and Physics*, *15*(20), 11,967–11,980. https://doi.org/10.5194/acp-15-11967-2015

He, C., Takano, Y., & Liou, K.-N. (2017). Close packing effects on clean and dirty snow albedo and associated climatic implications. *Geophysical Research Letters*, *44*, 3719–3727. https://doi.org/10.1002/2017GL072916

He, C., Takano, Y., Liou, K.-N., Yang, P., Li, Q., & Chen, F. (2017). Impact of snow grain shape and black carbon-snow internal mixing on snow optical properties: Parameterizations for climate models. *Journal of Climate*, *30*, 10,019–10,036. https://doi.org/10.1175/JCLI-D-17-0300.1

He, C., Takano, Y., Liou, K.-N., Yang, P., Li, Q., & Mackowski, D. W. (2016). Intercomparison of the GOS approach, superposition Tmatrix method, and laboratory measurements for black carbon optical properties during aging. *Journal of Quantitative Spectroscopy & Radiative Transfer*, *184*, 287–296. https://doi.org/10.1016/j.jqsrt.2016.08.004

Jin, Z., Charlock, T. P., Yang, P., Xie, Y., & Miller, W. (2008). Snow optical properties for different particle shapes with application to snow grain size retrieval and MODIS/CERES radiance comparison over Antarctic. *Remote Sensing of Environment*, *112*, 3563–3581. https://doi.org/10.1016/j.rse.2008.04.011

Kokhanovsky, A. (2013). Spectral reflectance of solar light from dirty snow: A simple theoretical model and its validation. *The Cryosphere*, *7*(4), 1325–1331. https://doi.org/10.5194/tc-7-1325-2013

Kokhanovsky, A., & Zege, E. (2004). Scattering optics of snow. *Applied Optics*, *43*, 1589–1602. https://doi.org/10.1364/AO.43.0001589

Krekov, G. M. (1993). Models of atmospheric aerosols. In S. G. Jennings (Ed.), *Aerosol Effects on Climate* (pp. 9–72). Tucson, AZ: University of Arizona Press.

LaChapelle, E. R. (1969). *Field Guide to Snow Crystals*. Seattle: University of Washington Press.

Lee, W.-L., Liou, K. N., He, C., Liang, H.-C., Wang, T.-C., Li, Q., … Yue, Q. (2017). Impact of absorbing aerosol deposition on snow albedo reduction over the southern Tibetan plateau based on satellite observations. *Theoretical and Applied Climatology*, *129*(3-4), 1373–1382. https://doi.org/10.1007/s00704-016-1860-4

Liou, K. N., Takano, Y., He, C., Yang, P., Leung, R. L., Gu, Y., & Lee, W. L. (2014). Stochastic parameterization for light absorption by internally mixed BC/dust in snow grains for application to climate models. *Journal of Geophysical Research: Atmospheres*, *119*, 7616–7632. https://doi.org/10.1002/2014JD021665

Liou, K. N., Takano, Y., & Yang, P. (2011). Light absorption and scattering by aggregates: Application to black carbon and snow grains. *Journal of Quantitative Spectroscopy & Radiative Transfer*, *112*, 1581–1594. https://doi.org/10.1016/j.jqsrt.2011.03.007

Liou, K. N., & Yang, P. (2016). *Light Scattering by Ice Crystals: Fundamentals and Applications* (pp. 168–173). Cambridge, UK: Cambridge University Press. https://doi.org/10.1017/CBO9781139030052

Magono, C., Endoh, T., Ueno, F., Kubota, S., & Itasaka, M. (1979). Direct observations of aerosols attached to falling snow crystals. *Tellus*, *31*, 102–114.

Marshall, S., & Oglesby, R. J. (1994). An improved snow hydrology for GCMs. Part 1: Snow cover fraction, albedo, grain size, and age. *Climate Dynamics*, *10*, 21–37.

Marshall, S. E. (1989). A physical parameterization of snow albedo for use in climate models, NCAR Cooperative Thesis 123 (175 pp.). Boulder, CO: National Center for Atmospheric Research.

Marshall, S. E., & Warren, S. G. (1987). Parameterization of snow albedo for climate models. In B. E. Goodison, R. G. Barry, & J. Dozier (Eds.), *Large Scale Effects of Seasonal Snow Cover*, *IAHS Publ* (Vol. 166, pp. 43–50). Washington, DC: International Association of Hydrological Sciences.

Menon, S., Koch, D., Beig, G., Sahu, S., Fasullo, J., & Orlikowski, D. (2010). Black carbon aerosols and the third polar ice cap. *Atmospheric Chemistry and Physics*, *10*, 4559–4571. https://doi.org/10.5194/acp-10-4559-2010

Ming, J., Wang, Y., Du, Z., Zhang, T., Guo, W., Xiao, C., … Yang, W. (2015). Widespread albedo decreasing and induced melting of Himalayan snow and ice in the early 21st century. *PLoS One*, *10*(6), e0126235. https://doi.org/10.1371/journal.pone.0126235

Mitchell, D. L., Macke, A., & Liu, Y. G. (1996). Modeling cirrus clouds. Part II: Treatment of radiative properties. *Journal of the Atmospheric Sciences*, *53*(20), 2967–2988. https://doi.org/10.1175/1520-0469(1996)053%3C2967:MCCPIT%3E2.0.CO;2

Mlawer, E. J., & Clough, S. A. (1997). On the extension of rapid radiative transfer model to the shortwave region. In *Proceedings of Sixth Atmospheric Radiation Measurement (ARM) Science Team Meeting, CONF-9603149* (pp. 223–226). Washington, DC: U.S. Department of Energy.

Nakamura, T., Abe, O., Hasegawa, T., Tamura, R., & Ohta, T. (2001). Spectral reflectance of snow with a known grain-size distribution in successive metamorphism. *Cold Regions Science and Technology*, *32*(1), 13–26. https://doi.org/10.1016/S0165-232X(01)00019-2

Oleson, K. W., Dai, Y., Bonan, G., Bosilovich, M., Dickinson, R., Dirmeyer, P., … Zeng, X. (2004). Technical Description of the Community Land Model (CLM). NCAR Technical Note NCAR/TN-461+STR, National Center for Atmospheric Research. https://doi.org/10.5065/D6N877R0

Painter, T. H., Flanner, M. G., Kaser, G., Marzeion, B., VanCuren, R. A., & Abdalati, W. (2013). End of the Little Ice Age in the Alps forced by industrial black carbon. *Proceedings of the National Academy of Sciences of the United States of America*, *110*(38), 15,216–15,221. https://doi.org/10.1073/pnas.1302570110

Qi, L., Li, Q., He, C., Wang, X., & Huang, J. (2017). Effects of the Wegener–Bergeron–Findeisen process on global black carbon distribution. *Atmospheric Chemistry and Physics*, *17*(12), 7459–7479. https://doi.org/10.5194/acp-17-7459-2017

Qi, L., Li, Q., Li, Y., & He, C. (2017). Factors controlling black carbon distribution in the Arctic. *Atmospheric Chemistry and Physics*, *17*(2), 1037–1059. https://doi.org/10.5194/acp-17-1037-2017

Qian, Y., Flanner, M. G., Leung, L. R., & Wang, W. (2011). Sensitivity studies on the impacts of Tibetan Plateau snowpack pollution on the Asian hydrological cycle and monsoon climate. *Atmospheric Chemistry and Physics*, *11*, 1929–1948. https://doi.org/10.5194/acp-11-1929-2011

Qian, Y., Gustafson, W. I. Jr., Leung, L. R., & Ghan, S. J. (2009). Effects of soot-induced snow albedo change on snowpack and hydrological cycle in western United States based on weather research and forecasting chemistry and regional climate simulations. *Journal of Geophysical Research*, *114*, D03108. https://doi.org/10.1029/2008JD011039

Qian, Y., Yasunari, T. J., Doherty, S. J., Flanner, M. G., Lau, W. K. M., Ming, J., … Zhang, R. (2015). Light-absorbing particles in snow and ice: Measurement and modeling of climatic and hydrological impact. *Advances in Atmospheric Sciences*, *32*(1), 64–91. https://doi.org/10.1007/s00376-014-0010-0

Räisänen, P., Makkonen, R., Kirkevåg, A., & Boldingh Debernard, J. (2017). Effects of snow grain shape on climate simulations: Sensitivity tests with the Norwegian Earth System Model. *The Cryosphere*, 1–41. https://doi.org/10.5194/tc-2017-118

Schwarz, J. P., Gao, R. S., Perring, A. E., Spackman, J. R., & Fahey, D. W. (2013). Black carbon aerosol size in snow. *Science Report UK*, *3*(1), 1356. https://doi.org/10.1038/srep01356

Takano, Y., & Liou, K. N. (1989a). Solar radiative transfer in cirrus clouds. Part I. Single-scattering and optical properties of hexagonal ice crystals. *Journal of the Atmospheric Sciences*, *46*(1), 3–19. https://doi.org/10.1175/1520-0469(1989)046%3C0003:SRTICC%3E2.0.CO;2

Takano, Y., & Liou, K. N. (1989b). Solar radiative transfer in cirrus clouds. Part II. Theory and computation of multiple scattering in an anisotropic medium. *Journal of the Atmospheric Sciences*, *46*(1), 20–36. https://doi.org/10.1175/1520-0469(1989)046%3C0020:SRTICC%3E2.0.CO;2

Takano, Y., Liou, K. N., Kahnert, M., & Yang, P. (2013). The single-scattering properties of black carbon aggregates determined from the geometric-optics surface-wave approach and the T-matrix method. *Journal of Quantitative Spectroscopy & Radiative Transfer*, *125*, 51–56. https://doi.org/10.1016/j.jqsrt.2013.04.006

Wang, X., Doherty, S. J., & Huang, J. (2013). Black carbon and other light-absorbing impurities in snow across northern China. *Journal of Geophysical Research: Atmospheres*, *118*, 1471–1492. https://doi.org/10.1029/2012JD018291

Wang, X., Pu, W., Ren, Y., Zhang, X., Zhang, X., Shi, J., … Chen, Q. (2017). Observations and model simulations of snow albedo reduction in seasonal snow due to insoluble light-absorbing particles during 2014 Chinese survey. *Atmospheric Chemistry and Physics*, *17*(3), 2279–2296. https://doi.org/10.5194/acp-17-2279-2017

Warren, S. G. (1982). Optical properties of snow. *Reviews of Geophysics and Space Physics*, *20*(1), 67–89. https://doi.org/10.1029/RG020i001p00067

Warren, S. G., & Brandt, R. E. (2008). Optical constants of ice from the ultraviolet to the microwave: A revised compilation. *Journal of Geophysical Research*, *113*, D14220. https://doi.org/10.1029/2007JD009744

Warren, S. G., & Wiscombe, W. J. (1980). A model for the spectral albedo of snow. 2. Snow containing atmospheric aerosols. *Journal of the Atmospheric Sciences*, *37*(12), 2734–2745. https://doi.org/10.1175/1520-0469(1980)037%3C2734:AMFTSA%3E2.0.CO;2

Warren, S. G., & Wiscombe, W. J. (1985). Dirty snow after nuclear-war. *Nature*, *313*(6002), 467–470. https://doi.org/10.1038/313467a0

Wiscombe, W. J., & Warren, S. G. (1980). A model for the spectral albedo of snow: I. Pure snow. *Journal of the Atmospheric Sciences*, *37*(12), 2712–2733. https://doi.org/10.1175/1520-0469(1980)037%3C2712:AMFTSA%3E2.0.CO;2

Ye, H., Zhang, R., Shi, J., Huang, J., Warren, S. G., & Fu, Q. (2012). Black carbon in seasonal snow across northern Xinjiang in northwestern China. *Environmental Research Letters*, *7*, 044002. https://doi.org/10.1088/1748-9326/7/4/044002

Zege, E., Katsev, I., Malinka, A., Prikhach, A., & Polonsky, I. (2008). New algorithm to retrieve the effective snow grain size and pollution amount from satellite data. *Annals of Glaciology*, *49*, 139–144. https://doi.org/10.3189/172756408787815004